Research Square

Preprints are preliminary reports that have not undergone peer review.
They should not be considered conclusive, used to inform clinical practice,
or referenced by the media as validated information.

An Intelligent Fiber-Shaped Photodetector Array Featuring High-Linearity Opto-Mechanical Response

Yanfang Meng

1000006368@ujs.edu.cn

Jiangsu University

Feng Sun

Jiangsu University

Tianchen ji

Jiangsu University

Longwei Li

Jiangsu University

Mengke Li

Jiangsu Normal University Kewen College

Wenyao Wu

Jiangsu University

Article

Keywords: High Linear strain-modulated photoelectric, fiber-shaped Photodetector array, Ai-enabled decoupled

Posted Date: November 11th, 2026

DOI: https://doi.org/10.21203/rs.3.rs-10985119/v1

License: This work is licensed under a Creative Commons Attribution 4.0 International License.
Read Full License

Additional Declarations: No competing interests reported.

An Intelligent Fiber-Shaped Photodetector Array Featuring High-Linearity Opto-Mechanical Response

Yanfang Meng[a,,+], Feng Sun[a,b,+] Tianchen ji[c], Longwei Li[d], Mengke Li[e], Wenyao Wu[c]*

[a] *Department of Mechanical and Electrical Engineering, School of Mechanical Engineering, Jiangsu University, Zhenjiang, China. No.301 Xuefu Road, Zhenjiang, Jiangsu Province, 212013*

[b] *Yongjiang Lab, Funct Mat & Device Heterogeneous Integrat Res Ctr, Ningbo 315202, Peoples R China*

[c] *Department of Optoelectronic Information Engineering, School of Mechanical Engineering, Jiangsu University, Zhenjiang, China. No.301 Xuefu Road, Zhenjiang, Jiangsu Province, 212013*

[d] *School of Materials Science and Engineering, Jiangsu University, Zhenjiang, China. No.301 Xuefu Road, Zhenjiang, Jiangsu Province, 212013*

[e] *Department of Artificial Intelligence, Jiangsu Normal University Kewen College, Xuzhou 221132, China*

**** Corresponding author***

Email address: 1000006368@ujs.edu.cn.cn

Abstract

The rapid evolution of artificial intelligence (AI) technologies is accelerating the development of fiber-based photodetectors (FPDs), driving further transformation and progress of the electronics industry. Nevertheless, the transition of FPDs from laboratory prototypes to viable daily-use technologies necessitates extensive research on multifunctional capabilities. Addressing this gap, we pioneer a highly intelligent strain-opto dual-mode sensing platform based on MoS_2/PEDOT:PSS heterojunction FPD array for wearable applications. Circumventing traditional vertical heterostructures that focus on piezoelectric-induced intensity enhancement, our work prioritizes linearity optimization through precise interfacial engineering. A key breakthrough of this work lies in the integration of PEDOT:PSS as a conductive pathway, which endows the device with

an exceptionally linear strain-dependent photocurrent response ($R^2 \sim 0.93$), thereby providing a reliable foundation for co-located photoelectric and mechanical sensing. First-principles calculations uncover that the higher-loaded PEDOT:PSS layer introduces uniformly distributed metal-induced gap states (MIGS) and stabilizes the Fermi level via pinning effects, ensuring that strain-induced band offsets modulate carrier transport in a strictly linear regime. Furthermore, to address the inherent signal coupling in practical wearable scenarios, a system-level AI-driven decoupling framework is implemented, enabling the resolution of complex, overlapping inputs into independent data streams with high fidelity.

Key words: High Linear strain-modulated photoelectric, fiber-shaped Photodetector array, Ai-enabled decoupled

Introduction

The rapid evolution of wearable electronics and artificial intelligence has propelled the advancement of flexible optoelectronic devices towards a new frontier, garnering extensive attention in cutting-edge intelligent applications such as bionic eyes, environmental monitoring, smart textiles, and optical communication. Of particular interest are fiber-shaped photodetectors (FPDs), which provide remarkable advantages including high flexibility, lightweight properties, omnidirectional light absorption capability, and intrinsic integration compatibility with textiles, rendering them uniquely suited for next-generation portable and wearable electronic systems. [1-6] Specifically, they overcome the limitations of planar photodetectors in efficiently absorbing incident light from multiple directions. [7-8] Current methodologies employed for the fabrication of fiber-based photodetectors encompass: surface coating, [9-10] wet spinning, [11-12] electrospinning, [3,13-14] and thermal drawing. [15,16] The application of photodetectors in wearable technology is a well-established field, involving 1D, 2D, 3D organic semiconductors, and hybrid semiconductors. [17-19]

Although current FPDs demonstrate excellent optoelectronic metrics, existing studies

have focused on the retention of optoelectronic performance under bending deformation. However, a comprehensive quantitative analysis on the relationship between photoresponse and strain of FPDs, remains underexplored, [20,21] substantially restricting further deepening and broadening their applications domain. Because, elucidating the functional relationships between the optoelectronic properties and strain is recognized to effectively bridge between high performance and real-world application for the implementation of multifunctional e-skins that integrate light and strain sensing, [22,23] a capability at the forefront of next-generation flexible electronics.

Therefore, the advancement of FPD architectures requires stringent criteria for exploring new materials and mechanistic understanding of the correlation between deformation and optoelectronic performance to realize a sophisticated FPD capable of multiplexed sensing. Among emerging candidate materials, the 2D materials have demonstrated a promising prospect. The intrinsic characteristic of layer-dependent transition from an indirect to a direct bandgap (Mak et al. 2010), [24] coupled with the efficient light absorption in ultra-thin films stemming from their direct bandgap and strong excitonic effects (Bernardi et al. 2013), [25] combined with the feasibility of monolithic flexible integration, unlocks new opportunities for the advanced intelligent and highly-integrated wearable devices. Therefore, the exploration of 2D materials, particularly, transition metal dichalcogenides (TMDs) has ushered a transformative era. Molybdenum disulfide (MoS_2), a premier among TMDs, [26] is widely used in fiber-based photodetectors (FPDs) [12,27-28] due to its excellent optoelectronic properties stemming from its electronic band structure and its atomic-scale thickness ideal for flexible electronics. [29-32] Despite extensive research on the strain-dependent optoelectronic properties of MoS_2-based photodetectors [33-36], harnessing the intrinsic mechano-sensitivity of MoS_2 for multifunctional FPDs remains a significant challenge. To fulfill the above demands and enhance the electrical conductivity and optoelectronic performance of MoS_2, hybridization or doping with PEDOT:PSS is commonly employed.

Recognizing the lack of quantitative models for dual-mode sensing under

deformation, we ingeniously developed a wearable photodetector based on (MoS_2)/PEDOT:PSS heterogeneous architecture by leveraging the synergistic advantages of MoS_2 and PEDOT:PSS in cutting-edge flexible electronics integration. [37-38] The core innovation is lies in the incorporation of PEDOT:PSS as a robust conductive network to achieve an exceptionally linear strain-dependent photocurrent response. Building upon this, we demonstrate a multifunctional wearable FPD for dual light-strain monitoring, establishing a foundation for advanced electronic skins. Combining cost-effectiveness and environmental sustainability with high controllability, our strategy furnishes researchers and engineers with valuable insights and a strategic roadmap for further innovations in the realm of FPDs with new functionalities. [39-42]

2. Results and Discussion

2.1 Fabrication and fundamental characterization

The schematic diagram of the operational concept of the proposed FPD array is shown in **Figure 1a**. Photoelectric signals from a monochromatic light source were detected by the body-worn photodetector array, followed by amplification, collection by a central module, and ultimate transmission to a mobile phone via Bluetooth. While drawing inspiration from the work of Chunhua An *et al.*—where a self-healing photodetector was designed by dispersing 2D materials sheets into a hydrogel film (Deng et al. 2020) [36]—we have developed an alternative fabrication strategy (with circuit diagram in **Figure 1b**), involving the dispersion of liquid-phase exfoliated MoS_2 nanosheets [43-44] homogeneously within a PEDOT:PSS and PVP/cellulose acetate spinning solution. Subsequent electrospinning forms a uniform active layer coating on commercial silver electrodes. The high transparency and negligible absorption of incident light ensure that the optoelectronic properties of the FPD remain uncompromised. The as-prepared MoS_2/PEDOT:PSS@PVP/cellulose acetate @ silver-yarn was interlaced in a crossbar configuration with another bare silver wire to create the heterojunction FPDs array (**Figure 1c**). Scanning electron microscopy (SEM) images illustrating the front and sectional views of the fabricated fiber units within the

integrated photodetector array are presented in **Figure 1 (enlarged image)** and **Figure S1**. Comparative SEM analysis (**Figures S1a–d**) reveals that the commercial silver yarn and as-prepared MoS_2/PEDOT:PSS@PVP/cellulose acetate @ silver-yarn and corresponding energy spectrum analysis (EDS). The comparative images in **Figure S1 (a)** and **S2(b)**, the commercial silver(a) and the diameter of electrospinning fiber's possess a uniform diameter along the yarn with a coating thickness (excluding the diameter of silver yarn core) of approximately 8 μm. A similar trend is observed in the sectional views presented in **Figure S1 (c) and S2(d)**. EDS analysis reveals distinct compositional differences. The commercial silver yarn shows a predominantly Ag signal in both its inner and outer layers (**Figure S1e, S2f**). In contrast, the electrospun fiber exhibits an Ag-rich outer layer (**Figure S1g**) but an inner layer composed mainly of C, N, O, Mo, and S, with minimal Ag present (**Figure S1h**), demonstrating the coexistence of MoS_2, PEDOT:PSS, PVP, and cellulose acetate. No peak is observed above a binding energy of 4 keV, indicating the absence of elemental impurities in the electrospinning sample.

The effects of the ratio of PEDOT:PSS-to-MoS_2 on the properties of the devices were systematically evaluated by comparing pristine MoS_2 with MoS_2/PEDOT:PSS composites having molar ratios of 20:1(referred to MoS_2/PEDOT:PSS(20:1) heterojunction) and 10:1(referred to MoS_2/PEDOT:PSS(10:1) heterojunction), respectively. (Based on the molecular weights of the MoS_2 unit, 160.06 g/mol, and the PEDOT:PSS repeat unit, 345.45 g/mol). Further details can be found in the experimental section. The thickness of the heterostructure is revealed by scanning electron microscopy (SEM, **Figure 1**) and transmission electron microscopy (TEM), as shown in **Figure S2**, respectively.

Atomic-resolution Cs-corrected STEM was employed to characterize the monoclinic nano-structures of pristine MoS_2, with energy spectrum analysis (*EDS*) elemental mapping spectroscopy illustrated in **Figure S2a**. The HAADF-STEM image in **Figure S2b** reveals a serpentine ordering of bright dots, attributed to the Mo atomic columns. The structure comprises hexagonal closely-packed Mo and S atomic units. The

single-crystal electron diffraction pattern in **Figure S2c** exhibits a highly ordered hexagonal arrangement of reflections, indicating a nearly defect-free, long-range ordered atomic structure in MoS_2. The lattice planes were identified as (002), (100), (103), (105), and (110). Furthermore, the corresponding elemental mappings of Mo and S (**Figure S2d**) confirm a uniform chemical distribution throughout the material [45]. The crystallographic plane diagram derived from the low-magnification STEM-HAADF image in **Figure S2** is shown in **Figure S3**.

High-quality quasi-centimeter-sized single crystals of MoS_2 were successfully fabricated via mechanical exfoliation of bulk MoS_2 and XRD tests demonstrate its high purity (**Figure S4**). In **Figure S4,** the pure-phase MoS_2 exhibits characteristic diffraction peaks at 14.8°, 29.8°, 44.2°, and 60.8°, which correspond to the (002), (100), (103), (105), and (110) crystal planes of MoS_2, respectively, and crystal planes are consistent with those determined by STEM in **Figure S2c**. Among these, the strongest peak at 14.8° indicates that the predominantly exposed crystal plane is (002) [46-47].

In terms of pristine MoS_2(**Figure 2a)**, the Mo 3*d* spectrum exhibits characteristic peaks at binding energies of 229.89 eV and 233.0 eV, corresponding to Mo^{4+} $3d_{5/2}$ and Mo^{4+} $3d_{3/2}$ of MoS_2, respectively. An additional peak observed at 236.18 eV is attributed to Mo^{6+} $3d_{3/2}$. The presence of Mo (VI) likely originates from the excess Mo precursor and its incomplete consumption during the synthesis, along with the unavoidable surface oxidation of MoS_2 upon exposure to air. [48] The intensified S 2*s* peak at 227.10 eV in **Figures 2b and 2c** corresponds to a higher sulfur concentration, confirming the successful introduction of PEDOT:PSS. [49] Notably, the identical Mo 3*d* spectrum of MoS_2/PEDOT:PSS(20:1) heterojunction and MoS_2/PEDOT:PSS(10:1) heterojunction in **Figures 2b** and **2c**, indicates that the PEDOT:PSS modification is non-invasive and does not perturb the electronic orbitals of MoS_2. S 2*s* spectra in *XPS* state of original MoS_2, MoS_2/PEDOT:PSS(20:1) composite, and MoS_2/PEDOT:PSS (10:1) composite illustrate in **Figure S5.** In the S 2*p* spectrum, the double peaks located at 162.7 eV and 163.9 eV are assigned to S $2p_{3/2}$ and S $2p_{1/2}$ of MoS_2, respectively.

The band gap energy of the semiconductor can be determined through

combined-multi-method, including ultraviolet photoelectron spectroscopy (*UPS*), valence band X-ray photoelectron spectroscopy (*VB-XPS*), and *Tauc* plot analysis derived from ultraviolet-visible diffuse reflectance spectroscopy (*UV-Vis* DRS). [50] **Figure 2d** and **Figure 2e** illustrate the UPS of pristine MoS_2 and MoS_2/PEDOT:PSS composite, with the band information inserted. The incorporation of PEDOT:PSS induces minimal variation of the band of the pristine MoS_2. The *UV–Vis–NIR* absorption spectra of MoS_2, MoS_2/PEDOT:PSS(1) and MoS_2/PEDOT:PSS-(2) are illustrated in **Figure S6**, with a the extracted *Tauc* curves inserted in Figure S6, indicated that the bandgap of pristine MoS_2 and MoS_2/PEDOT:PSS-(2) were ≈ 2.15 eV (The derivation process is provided in the Supporting Information). The close similarity in the *Tauc* curves spectra between the MoS_2/PEDOT:PSS heterojunction and pristine MoS_2 (Figure S6) combining with the close similarity in the *VB*-XPS spectra (**Figure S7**, the bandgap of pristine MoS_2 and MoS_2/PEDOT:PSS-(2) were ≈ 1.95 eV) demonstrate that PEDOT:PSS has no impact on the fundamental band structure of the original MoS_2. It is noteworthy that previously reported bandgap modulation in MoS_2 by PEDOT:PSS relied on semiconductor processing techniques that allowed the polymer to infiltrate and interact with the crystal lattice of MoS_2. In contrast, our approach is non-invasive, the PEDOT:PSS and MoS_2 remain as distinct, independent semiconductors within the heterojunction. [51] Before investigating the optical performance, the transfer curve of MoS_2/PEDOT:PSS heterojunction has been carried out (**Figure 2f**), with calculated subthreshold swing (*SS*)(85 mV/dec) from transfer curve inserted, at a source-drain voltage of 2 V. [52] The electronic properties of the device are dictated by the n type-MoS_2/p-type PEDOT:PSS heterojunction.

2.2 Photoelectric characterization

2.2.1 Photoelectric characterization of planar-configuration device

Prior to investigating the fiber-based heterojunction photodetectors (FPDs), planar-configuration devices were first fabricated and characterized (Detailed preparation process can be found in the Supporting Information). **Figure 3a** shows a schematic illustration of the MoS_2/PEDOT:PSS(20:1) planar-configuration

heterojunction device.

As shown in **Figure 3b**, the photocurrent of MoS_2/PEDOT:PSS(20:1) heterojunction systematically increases with an increment of optical power, as evidenced by the *I-V* curves recorded across different power levels. **Figure S8** shows the voltage-dependent photocurrent of the three devices—pristine MoS_2, MoS_2/PEDOT:PSS(20:1) heterojunction, and MoS_2/PEDOT:PSS(10:1) heterojunction—measured at the three different wavelengths with the photocurrents of PEDOT:PSS-containing samples exhibiting superiority over the pristine MoS_2.

Figure 3c manifests that the photocurrent of all three samples conform to a power-law dependence on the incident optical power(P). At a bias voltage of 0.01 V and a power density range of 1-10 mW/cm^2, the extracted $I \sim P$ relationship of original MoS_2-based device, MoS_2/PEDOT:PSS(20:1) -based device, and MoS_2/PEDOT:PSS(10:1)-based device can be expressed as $I \sim 0.0008P^{0.795}$, $I \sim 0.0008P^{0.938}$, and $I \sim 0.0008P^{0.787}$. The calculated power indices align closely with literature values, which validate the feasibility of our device. [53] Specifically, the photocurrent in **Figure 3b** is approximately two orders of magnitude higher than that in **Figure 3c**, being consistent with the fact that the power density in **Figure 3b** is two orders of magnitude greater than that in **Figure 3c**. The comparative evaluation of photoresponsivity (*R*) of pristine MoS_2-based device, MoS_2/PEDOT:PSS(20:1) -based device, and MoS_2/PEDOT:PSS(10:1)-based device across varying power intensity at 365 nm (157 μW/cm²) is displayed in **Figure 3d** (bias voltage 0.01 V). The photoresponsivity(R) of the above three samples across varying power intensity at 405 nm (203.7 μW/cm²) and 532 nm (236 μW/cm²) are displayed in **Figure S9** (a bias voltage of 0.01 V). Both **Figure 3d** and **Figure S9** make it evident that among the three samples MoS_2/PEDOT:PSS-(10:1) -based device exhibits the highest photoresponsivity.

Figure 3e presents the measured $I \sim V$ characteristics of three samples under similar incident power levels (-1 V ～ 1 V, the specific power densities varied slightly between the given wavelengths, 365 nm at 315 μW/cm², 405 nm at 331.04 μW/cm², and 532 nm at 364 μW/cm²). The observed inverse relationship between photocurrent and

wavelength under constant optical power is attributed to the lower photon energy of longer wavelengths.

As a key performance metric for photodetectors, detectivity(D^*) can be expressed as:

$$D^* = \frac{J_l - J_d}{P\sqrt{2eJ_d}} \quad \text{.....(1)}$$

Where, J_l, J_d,P, and e, represent the photocurrent, dark current, power intensity, and electron charge, respectively.

D^* values of the above three samples across varying power intensity at 365 nm (at the power density of 66.3 mW/cm^2, 315.35 mW/cm^2, 473.19 mW/cm^2, 847.53 mW/cm^2, and 1078.86 mW/cm^2) and 405 nm (at the power density of 66.2 μW/cm², 203.72 μW/cm², 366.69 μW/cm², 509.29 μW/cm², and 687.55 μW/cm² (bias voltage 0.01 V) is displayed in **Figure 3f** and **Figure 3g**, respectively. Similarly**, the relationship of the** D^* the power density of the samples at 532 nm 532 nm (152 μW/cm², 236 μW/cm², 364 μW/cm², 488 μW/cm², and 608 μW/cm²) are shown in **Figure S10**. As shown in **Figures 3f and Figure S10**, D^* decreases with rising optical power for all samples. Notably, at any given intensity and wavelength, the detectivity follows the sequence MoS_2/PEDOT:PSS-(2)-based device > MoS_2/PEDOT:PSS(1)-based device > pristine MoS_2-based device, demonstrating that the introduction of PEDOT:PSS greatly improves detectivity, alongside the maximum detectivity achieved by the MoS_2/PEDOT:PSS-(2) device at at 405 nm, highlighting the optimal response of the heterojunction at this wavelength.

Figure 3h compares the photoresponsivity (R) and detectivity D^* as a function of intensity between devices for three types of devices. The MoS_2/PEDOT:PSS(10:1) heterojunction showed significant enhancement over pristine MoS_2: resulting in enhancements of 88% in photoresponsivity and 31.7% in detectivity, In comparison, MoS_2/PEDOT:PSS(20:1) heterojunction exhibited improvements these gains to 17% and 26.2%, respectively.

External quantum efficiency (EQE) is defined as the ratio of the number of photogenerated charge carriers to the number of incident photons. It can be derived from the responsivity with the expression as following:

$$\mathrm{EQE} = \frac{R_\lambda hc}{e\lambda} \qquad \ldots\ldots\ldots\ldots\ldots\ldots\ldots\ldots(2)$$

Where, *R, h, c, e,* and λ refer to the responsivity, Planck's constant, the speed of light, the electron charge, and the wavelength of the incident laser, respectively. To evaluate this metric, **Figure S11** characterizes the power-dependent EQE under the 365(a) 405(b), and 532(c) and at a bias voltage of 0.01 V. In addition to the improved D^* and *R*, the MoS_2/PEDOT:PSS heterojunction device shows a significantly higher EQE than untreated MoS_2 counterpart. Real-time photocurrent monitoring (**Figure S12**) confirms the excellent stability of the devices under 365nm, 405nm, and 532 nm illumination, validating the principle that photocurrent scales with increasing optical power. **Figure S13** compares the real-time photocurrent of the pristine MoS_2-based device with that of the MoS_2/PEDOT:PSS(20:1)-based device and MoS_2/PEDOT:PSS-(10:1)-based device, under the 405nm (b) and 532nm(c) and a bias voltage of 0.01 V. Among these, the MoS_2/PEDOT:PSS(20:1) heterojunction achieves the highest photocurrent. In addition to its power dependence, the device's photocurrent is also voltage-dependent. Measurements at 405 nm and 66.3 mW/cm² (**Figure S14**) show that the photocurrent increases with voltage and then plateaus beyond 0.1 V.

The underlying mechanism for the photocurrent generation is shown in **Figure 3i.** The band alignment between MoS_2 and PEDOT:PSS induces a band bending at the heterojunction interface. Under optical illumination, electrons occupying trap states in MoS_2 are photoexcited and subsequently extracted by the built-in electric field. The resulting positively charged sulfur vacancies enhance band bending through a photodoping effect, which simultaneously thins the *Schottky* barrier and persistently facilitates charge transport across the junction. Under an applied electric field, the collective drift of conduction band electrons and valence band holes ultimately generates the measured photocurrent.

2.2.2 Photoelectric characterization of FPD

While previous extensive studies have reported the fabrication of large-scale optoelectronic fabrics using advanced processing techniques, a systematic investigation of integrated auxiliary functionalities—such as strain monitoring—remains lacking. [54]

Although Xin Tang *et al.* have also reported the strain-modulated photoresponse of 2D MoS_2/PEDOT:PSS PD device. Notably, the on-chip configurations pose integration challenges for wearable applications compared to fiber-based architectures. Meanwhile, the lack of quantitative analysis regarding response linearity and the influence of PEDOT:PSS loading levels limits the precise control of such hybrid systems. [55] This presents a crucial opportunity for further research, particularly given the burgeoning trend toward multifunctional wearable electronics. Our FPD device addresses these limitations, and prioritizes high-linearity performance through interfacial electronic optimization. A schematic of the strained heterojunction structure under mechanical bending is presented in **Figure 4a**.

The critical function of PEDOT:PSS is demonstrated by the control experiments. The photocurrent generated by the pristine MoS_2-based FPD (**Figure S15** left panel) remained at the noise floor, underscoring that PEDOT:PSS is essential for effective photodetection. The minimal photoresponse of the pristine device is attributed to the polymer matrix preventing effective electrical contact with the photoactive MoS_2 (As shown in **Figure 4a** upper panel). Drawing inspiration from strategies using metal nanowires to create conductive networks in 2D materials, [56-58] we introduced PEDOT:PSS to form a MoS_2/PEDOT:PSS heterojunction FPD. This device shows a distinguishable photoresponse (**Figure S15**, right panel) at a bias of voltage 0.01 V, because the PEDOT:PSS serves a dual role: forming a heterojunction and establishing percolation pathways for charge transport (as shown in **Figure 4a** bottom panel). Notably, its sensitivity remains four orders of magnitude lower than that of its planar counterparts. While strain effects in MoS_2 photodetectors have been reported, [34-36] the strain-dependent photoelectronic performance of the MoS_2/PEDOT:PSS heterojunction device under tensile strain has not been systematically discussed previously. As the pristine MoS_2-based FPDs exhibited no measurable photoresponse due to electrical isolation, they were excluded from further consideration.

The cylindrical cross-section of the device fibers combined with the alternating staggered arrangement of adjacent fibers induces optical losses due to shadowing effect.

As illustrated in **Figure S16**, when the active-layer-coated fiber is positioned below the uncoated fiber (left panel), a portion of the light incident on the contact interface is blocked by the overlying uncoated electrode, resulting in a reduction of the effective illumination area and thus a photocurrent loss. Conversely, when the active-layer-coated fiber is on top (right panel), part of its own contact interface is self-shadowed, leading to a similar loss mechanism. Based on the SEM images (**Figure S1**), which show negligible coating thickness and minimal changes in wire diameter, we conclude that geometric shadowing area remains largely unaffected. The comparable magnitudes of these two loss types—supported by simulation analysis—validate the assumption that they mutually offset each other. Consequently, we calculated the photocurrent loss under the assumption of uniform loss per unit cell across the array.

Figures 4b and **Figures 4c** present the voltage-dependent photocurrent of the MoS_2/PEDOT:PSS heterojunctions with molar ratios of 20:1 and 10:1 under 365 nm illumination (157 mW/cm²) while subjected to varying bending curvatures (curvature radii:17.94 m^{-1}, 21.69 m^{-1}, 28.01 m^{-1}, and 38.71 m^{-1}). **Figure S17** displays voltage-dependent photocurrent of the devices under 532 nm under equivalent bending conditions. Notably, the photocurrent of the MoS_2/PEDOT:PSS(10:1)-based device significantly exceeds that of its 20:1 counterpart, demonstrating that increased PEDOT:PSS loading enhances the conductive bridging effect and facilitates more efficient charge transport. Given that the photocurrent is four orders of magnitude lower than that of planar devices, and considering that both specific detectivity (D^*) and R are directly proportional to the photocurrent, we have omitted a detailed discussion of the D^* and R values for the fiber-based devices in this context. Here, the photo-strain responsivity is defined as the functional dependence of the relative current change on the bending curvature ($\Delta I/I_0$). A clear strain dependence of the photocurrent is observed under positive bias, whereas it is virtually insensitive to deformation under negative bias.

$$R = \frac{\Delta I_{strain}}{\Delta L_{strain}} \qquad \text{.....(3)}$$

The sensitivity of the photocurrent to bending strain is defined as the relative change

in photocurrent per unit of bending strain (curvature radius). As shown in **Figure 4d** (365 nm) and **Figure S18** (405 nm and 532 nm, at a bias voltage of 0.01 V), the calibrated photocurrent exhibits a linear dependence on the applied strain, confirming the device's potential for practical wearable strain sensing.

As revealed by the real-time photocurrent tests in **Figure 4e** (under 405 nm, 66.3 mW/cm^2), the device exhibits a pronounced strain response, with the current increasing proportionally with bending. Notably, the photocurrent magnitude is also four orders of magnitude lower than that of planar heterojunctions.

A comparative analysis in **Figure 4f** demonstrates the superior performance of the MoS_2/PEDOT:PSS(10:1) heterojunction device over MoS_2 device, which exhibits an enhanced response compared to the 20:1 counterpart.

Stability tests conducted over 500 bending cycles, at a given curvature radius of 17.94 m^{-1} and under a bias voltage of 0.01 V (**Figure S19**), reveal negligible degradation in the photocurrent (I_{ph}), demonstrating robust operational endurance. The photocurrent exhibits a slight initial drift (approximately 8% decrease) during the first 100 cycles, which is attributed to the mechanical relaxation and interfacial adaptation of the PEDOT:PSS conductive network and the polymer matrix, rather than permanent material degradation or delamination. This interpretation is supported by the fact that the photocurrent stabilizes after 150 cycles, with a total degradation of less than 12% over the entire 500 cycles. Furthermore, the device demonstrates excellent environmental stability, as confirmed by a two-month durability test under humid conditions (**Figure S20**).

To elucidate the physical origin of the enhanced strain-dependent sensitivity driven by increasing PEDOT:PSS concentrations, we systematically investigated the interfacial charge carrier dynamics using temperature-dependent electrical characterizations [59] on both MoS_2/PEDOT:PSS(20:1) and MoS_2/PEDOT:PSS(10:1) heterojunction devices. Comparative analysis has been conducted on the temperature-dependent current-voltage (*I-V*) curves of MoS_2/PEDOT:PSS heterojunction devices with ratios of 20:1 and 10:1 (**Figure 5a** and **5d**), respectively, under a planar configuration. The extracted *Schottky*

barrier heights(*SBH*) are 638 meV and 627 meV. (It can be assumed that the electrospun PVP matrices remain electrochemically inert under ideal conditions. Ten comparative experiments were conducted to confirm that the presence of the electrospun PVP does not influence the strain-dependent *Schottky* barrier behavior of the MoS_2/PEDOT:PSS(20:1) and MoS_2/PEDOT:PSS(10:1) heterojunction devices in this system.) Based on the standard 2D thermionic emission model, *Arrhenius* plots of $\ln\left(\frac{I_{ds}}{T^{3/2}}\right)$ versus $\frac{1}{T}$ were constructed. As shown in **Figure 5a-5c**, the extracted data reveal a distinct reduction in the effective *SBH*—from approximately 638 meV to 569 meV—under varying strains of 0 m^{-1}, 17.94 m^{-1} and 21.69 m^{-1}. As shown in **Figure 5d-5f**, the extracted data reveal a distinct reduction in the effective *SBH*—from approximately 627 meV to 534 meV—under varying strain range across from 0 m^{-1}, 17.94 m^{-1} to 21.69 m^{-1}. Both the MoS_2/PEDOT:PSS (20:1) and (10:1) composites exhibit a reduction in Schottky barrier height under bending strain, aligning with the observed photocurrent enhancement. Notably, this strain-induced barrier reduction is more pronounced in the 20:1 sample. The mechanism underlying this phenomenon can be attributed to the enhanced mechanical-electrical coupling at the interface. When mechanical strain is applied, the highly compliant nature of the PEDOT:PSS conductive network enhances mechanical coupling, facilitating a more pronounced structural deformation at the van der Waals gap between the organic layer and the MoS_2. Given that bulk MoS_2 is inherently centrosymmetric and lacks macroscopic piezoelectricity, the observed strain-induced modulation cannot be attributed to a conventional bulk piezo-phototronic effect. [60-62]

The mechanism underlying the superior strain sensitivity of MoS_2/PEDOT:PSS(10:1) heterojunction over MoS_2/PEDOT:PSS(20:1) heterojunction device was elucidated using Kelvin probe force microscopy (KPFM) (**Figure S21**). KPFM characterization reveals that the surface potential of MoS_2/PEDOT:PSS(20:1) device is 154.2 mV in its planar configuration (inserted in **Figure S21a**) and 449.6 mV under bending (curvature radius 17.81 m^{-1}) (inserted in **Figure S21b**). In contrast, the MoS_2/PEDOT:PSS(10:1) heterojunction reaches 234 mV in the planar state (**Figure S21c**) and surges to 803.3

mV under the same bending condition (**Figure S21d**). In all, under identical bending strain, the MoS_2 heterojunction with higher PEDOT:PSS loading exhibits a larger variation in surface potential.

First-principles calculations for the case of high PEDOT:PSS-loaded device have further reinforced this conclusion. Self-Consistent Field (SCF) calculations analysis indicates that the functionalization of MoS_2 with PEDOT:PSS is chemically non-invasive, preserving the intrinsic electronic orbitals and crystal integrity of the MoS_2 lattice. Nevertheless, from the perspective of physical interface level, a higher PEDOT:PSS-loading effectively modulates the band alignment through interfacial dipole formation. Although the quasi-particle band gap of MoS_2 itself remains relatively stable, its absolute position relative to the vacuum level shifts significantly due to the established interfacial dipole layer. [63] The comparative analysis of density of states (*DOS*) (**Figure 5g**) and the electronic band structures along the high-symmetry Γ-X-M-Γ path (**Figure 5h**) illustrated for MoS_2/PEDOT:PSS(20:1) device and MoS_2/PEDOT:PSS(10:1) device shows that at a high loading of PEDOT:PSS, metal-Induced gap states (*MIGS*) emerge within the band gap of MoS_2. [64] *DOS* comparison in **Figure 5g** reveal that as the concentration of PEDOT:PSS increases, Fermi level pinning occurs, where the overall Fermi level of the composite system progressively shifts toward the HOMO level of PEDOT:PSS, leading MoS_2 to exhibit more pronounced p-type doping characteristics.[65] The heterojunction of MoS_2/PEDOT:PSS(20:1) exhibits a distinct electronic band profile with the conduction band minimum (CBM) 2.8 positioned at the M point, yielding a fundamental band gap (Eg) of 0.19. Remarkably, when the loading of PEDOT:PSS increases to a 10:1 ratio (Figure 5h right panel) , the band dispersion curves are modified, resulting in an altered band gap of 0.41. This band reconfiguration and the modulated energy dispersion at the Γ-X-M sections effectively flatten/steepen the local potential barrier, which not only lowers the effective mass of photo-excited carriers, alongside providing a stronger thermodynamic driving force for spatial charge separation. This electronic optimization fundamentally is responsible for the accelerated carrier extraction and highly linear

opto-mechanical performance under external strain fields These induced states effectively facilitate the linear transport of charge carriers during mechanical deformation, ultimately facilitating the linearization of the opto-mechanical response and optimizing the device's sensing performance. [66] **Importantly, the insulating polymer matrix in the spinning solution, including PVP, acts solely as a macroscopic structural scaffold and does not perturb this fundamental interfacial electronic mechanism**.

Consequently, the MIGS do not generate the piezoelectric effect, rather, they function as a vital electronic buffer that regulates it, ensuring that the overall piezo-phototronic response maintains a relatively high linearity ($R^2 \sim 0.93$). Importantly, first-principles calculations demonstrate that increasing the PEDOT:PSS loading deepens the Fermi level pinning (enhancing the p-type characteristics) and substantially reinforces the MIGS network. The 10:1 ratio provides a substantially denser and more robust network of quasi-1D hole-transport pathways. This highly compliant conductive network serves as an excellent transport matrix that efficiently collects and stabilizes the polarization charges, thereby mitigating carrier recombination and minimizing the initial contact resistance. Consequently, for the 10:1 device, an equivalent magnitude of mechanical strain is successfully translated into a much larger surface potential variation and a significantly higher photocurrent output.

2.3 Intelligent Soft Sensing from 3D Strain Mapping to AI-Driven Robust Dual-Mode Perception

The outstanding linearity of the device facilitates its seamless integration into functional arrays, making it highly suitable for photoelectric-strain dual-sensing. Based on the optical losses analysis in **Figure S16**, which assumes uniform occlusion loss across adjacent units, it is evident the occlusion does not adversely influence neighboring units. As shown in **Figure 6a**, a 7×8 pixel array was fabricated to demonstrate detection of object shapes and separation distances. Prior to sensing approaching objects, the photoelectric performance of each unit in the matrix was

characterized. All 56 devices functioned properly, exhibiting minimal deviations (current variation < 5%). Representative output characteristics are shown in **Figure S22**, underscoring the array's robustness for subsequent topographic mapping.

The upper-left panel of **Figure 6a** shows a photograph of the device conformally attached to the elbow joint. Signals are collected by an integrated system comprising an *Omni-λ3045i* monochromator coupled with a 2450 *SourceMeter* (upper right panel). These signals are determined by the equivalent terminal voltage applied to the ends of the crisscrossing fibers. The collected signals were amplified by a signal converter and transmitted via Bluetooth (bottom right panel) to a mobile receiver. The output photocurrents were measured and visualized in a 3D color coordinate map (**Figure 6b**). The extracted strain distribution (**Figure 6c**) at different locations of the elbow joint can be independently resolved form the corresponding output current of each unit without cross-talk interference, which is crucial for low-power sensing applications. The practical strain monitoring capability of the FPD array is further validated by COMSOL simulations (**Figure 6d**), which show a 3D strain distribution on an elbow model that is closely aligned with experimental data **(Figure 6c)**, thereby validating the array's reliability in mapping stress and strain distribution under the specified load.

Existing decoupling methods include passive decoupling design based on distinct physical mechanisms (piezoionic effect + thermochromic effect) [67] and temporal machine learning-based signal separation algorithm (e.g. Long Short-Term Memory (LSTM) with local attention, [68] data-driven strategy [69], and Bioinspired Multimodal Tactile Fusion (BMTF) network [70]). However, these are fundamentally limited by relatively slow response and recovery dynamics, [68] low accuracy, [69] or heavily reliance on physically separated sensing channels, [70] respectively. These limitations in **handling weak signals** and slow response times underscore the challenges in achieving robust, real-time multimodal decoupling. Consequently, this motivates the exploration of more sophisticated artificial intelligence (AI)-driven decoupling strategies. We propose a multi-task neural network based on shared-branch architecture (MultiTaskSensorNet) for decoupled joint prediction of light intensity and strain signals.

Figure 6e illustrates the principle of the framework architecture for decoupling in deep learning. The input is defined as a vector **x** composed of two sensor signals, with $\mathbf{x} \in \mathbb{R}^2$. The model successfully maps the input to a high-dimensional feature space and extracts shared feature representations through two fully connected layers with nonlinear activation functions. This process can be presented as:

$$h = f_{shared}(x) = \sigma(W_2\,\sigma(W_1 x + b_1) + b_2) \quad \ldots\ldots\ldots\ldots\ldots\ldots\ldots\ldots(3)$$

Where W_1, W_2 and b_1, b_2 represent the weight matrices and biases of the shared layers, respectively, and $\sigma(\cdot)$ denotes the nonlinear ReLU activation function. Based on these shared layers, the model learns latent shared feature representations common across different tasks. Building on this shared representation, the model incorporates two independent task branches, for predicting light intensity and strain, respectively. Both branches take the shared feature **h** as input and consist of two fully connected layers. The detailed derivation process can be found in the Supporting information. **Figures 6f and Figure 6g** display signal decoupling under varying bending strain: the prediction accuracies reach 99% and 96% for light intensity standard values (**Figure 6f**) and prediction of strain standard values (**Figure 6g**), respectively, providing quantitative decoupling of continuous physical variables. In all, the model leverages shared information while achieving feature decoupling through task-specific branches, thereby effectively reducing overfitting and improving generalization for **handling weak signals**.

3 Conclusion

In summary, this work pioneers a multifunctional intelligent fiber-based photodetector (FPD) that exhibits an unprecedented, highly linear opto-mechanical response, diverging from traditional research focused solely on intensity enhancement. By strategically engineering the MoS_2/PEDOT:PSS heterojunction through a scalable electrospinning process, the device delivers robust photodetection metrics—including a responsivity of 10 A W^{-1}, an external quantum efficiency of 8.8%, and a specific

detectivity of 1.14 × 10^{10} Jones—alongside a crucial breakthrough in sensing linearity. First-principles calculations validate that this high linearity stems from the emergence of metal-induced gap states (MIGS) and robust fermi level pinning at the interface, guaranteeing that mechanical strain modulates carrier transport through a steady, linear regime.

Crucially, it transcends the functional limitations of traditional FPDs by intrinsically coupling optoelectronic performance with a novel self-decoupling strain-sensing capability—a long-standing challenge in multifunctional wearable sensors where signals are typically entangled. By transcending the limitations of traditional non-linear coupled sensing, this FPD array establishes a new paradigm for interference-free, multi-modal perception. Our cost-effective, scalable fabrication methodology establishes a new paradigm for developing multifunctional wearable electronics, paving the way for next-generation smart textiles and advanced human-machine interfaces. Our subsequent efforts will focus on developing mechanically robust, transparent electrode yarns for woven arrays, to minimize light occlusion within the textile architecture.

.

Experimental Part

1 Materials

Bulk MoS_2 powders were purchased from Six-Carbon Company, 10% NaOH, were purchased from *Sinopharm Reagent* Company. PEDOT:PSS, Polyvinyl Pyrrolidone (PVP), ethyl cellulose, and Dimethyl Formamide (DMF) were supplied by *Innochem* Company. The silver yarn was purchased from *Butterfly Centennial Brand* Company. Materials and reagents all achieve lab grade without any further purification. For all experiments, deionized water was used.

2 Methods

(1) Formulation of the MoS_2 Sheet

Bulk MoS_2 powder (0.2 g) was dispersed in 100 mL 10 wt% NaOH solution and stirred at room temperature for 12 hours. The mixture was then slowly evaporated to dryness at 90 °C. After drying, 10 mL of deionized water was added, and the entire

process was repeated three times. The resulting product was thoroughly washed with deionized water to remove residual NaOH. Finally, the sample was re-dispersed in 20 mL of ethanol and centrifuged at 1000 rpm for 1 minute to discard unexfoliated bulk aggregates.

(2) Preparing MoS_2/PEDOT:PSS complex aqueous solution

A given amount of MoS_2 sheet (0.093 g corresponds to 20:1 device; 0.186 g corresponds to 20:1 device) was dispersed into 1 ml commercial 2% PEDOT:PSS aqueous solution. **This dosage was determined based on** MoS_2 sheet to PEDOT:PSS (repeat unit) molar ratios of 10:1 and 20:1, alongside the molecular weights of the MoS_2 unit and the PEDOT:PSS repeat unit 160.06 and 345.45 g/mol, respectively. The suspension was ultrasonicated for 30 minutes to ensure uniform dispersion.

(3) Formulation of the MoS_2/PEDOT:PSS spinning solution

A homogeneous spinning solution (14 wt%) was prepared by dissolving polyvinylpyrrolidone (PVP) and ethyl cellulose at a 7:3 mass ratio in N,N-dimethylformamide (DMF). After the mixture was magnetically stirred at 200 rpm for five days under ambient conditions, 10 wt% (relative to the above spinning solution) MoS_2/PEDOT:PSS composite solution was added.

(4) FPD Device fabrication

The as-prepared solution was then loaded into a syringe equipped in the laboratory-scale electrospinner (2.2D-500Yflow), and uniformly electro-spun onto a commercially available silver yarn (diameter: 0.08 mm). To ensure conformal, full circumferential contact, the silver yarn was suspended on the roller of the electrospinning apparatus during the process, forming a semiconducting/ethyl cellulose-coated silver yarn, which was then interlaced in a crossbar configuration with another bare silver wire to produce the final FPD device.

(5) Planar-configuration devices fabrication

Prior to investigation of MoS_2/PEDOT:PSS-based FPD, planar-configuration devices were fabricated for initial characterization. First, MoS_2 flakes were mechanically exfoliated and transferred onto a heavily doped silicon. Subsequently, the desired

channel pattern was defined via electron beam lithography (EBL). A single droplet of PEDOT:PSS solution was then carefully drop-casted onto the pre-patterned MoS_2 flake under microscopic guidance, forming a well-defined MoS_2/PEDOT:PSS heterojunction. Following this, a second EBL step was performed to pattern the top source and drain electrodes. Finally, gold electrodes were deposited via thermal evaporation, followed by a standard lift-off process to remove excess metal, creating a patterned Au/MoS_2/PEDOT:PSS planar-configuration photodetector.

3 Characterization

The relative content of the O_{II} component in the O 1*s* orbital of the planar MoS_2 thin film and MoS_2/PEDOT:PSS heterojunction was ascertained by X-ray photoelectron spectroscopy (XPS), EXCALAB QXi. Electrical measurements were performed on the MoS_2 substrate after coating with a formulated PEDOT:PSS ink and subsequent drying in vacuum, therefore, the interaction between PEDOT:PSS and MoS_2 is non-invasive, involving physical contact without disrupting the MoS_2 lattice.

Ultraviolet Photoelectron Spectroscopy (UPS) is measured by Thermo fisher scientific ESCALAB XI^+, America.

The morphology and monoclinic nano-structures of pristine MoS_2 were performed on a Talos F200X G2 high-resolution transmission electron microscope (HRTEM) operated at an accelerating voltage of 200 kV, complemented by energy-dispersive X-ray spectroscopy (EDS) elemental mapping and selected area electron diffraction (SAED) analysis.

The crystalline characteristics of the MoS_2 thin film were characterized by X-ray diffraction (XRD, X'Pert³ MRD) with a 2θ scanning range of 10°–60°. (CuKα ray, tube current 35 mA, tube voltage 40 kV, scanning speed 8°/min)

UV–Vis–NIR absorption spectrum is measured by *Shimadzu* UV2600 across the wavelength range of 200 nm to 1800 nm.

The complex refractive index and dielectric functions of the MoS_2 and MoS_2/PEDOT:PSS composite thin film were measured using a spectroscopic ellipsometer (RC2) over a wavelength range of 200-1100 nm. Photoelectrical

measurements were carried out with an integrated system incorporating an Omni-λ3045i monochromator and a 2450 SourceMeter. For photoelectric response measurements, a laser pointer with a wavelength of 365nm, 408nm, and 532 nm with a power density of a 2.55 mW/cm^2, with tunable pulsed illumination controlled by an STM32 microcontroller.

To quantitatively map the surface potential (also known as contact potential difference, CPD) of a sample with high spatial resolution, Surface Potential Measurement conducted using Kelvin Probe Force Microscopy (KPFM) (*Bruker Innova*). The electrostatic force between a conductive AFM tip and the sample surface, a nulling technique is applied to directly determine the potential difference by compensating for it with an applied DC bias. Owing to the softness and inferior flatness of the sample conformed to the curved surface compared to a silicon wafer, the KPFM tip was operated in a gentle tapping mode with a soft engagement.

4 COMSOL Multiphysics Simulation

The simulation of stress distribution in the elbow joint is conducted using COMSOL, with the computational procedure encompassing: geometry reconstruction and meshing, Material properties and physics setup, and solving and postprocessing.

ASSOCIATED CONTENT

Supporting Information.

The Supporting Information is available free of charge on the ACS Publications website at DOI:

Part 1: The extracted *Tauc* curves from UV–Vis–NIR absorption spectrum

Part 2: The calculated subthreshold swing(*SS*) from transfer curve

Part 3: COMSOL Multiphysics Simulation

Part 4: The detailed derivation process for AI-enabled decoupled.

Part 5: Supplementary Figures.

AUTHOR INFORMATION

Corresponding Authors

*E-mail: 1000006368@ujs.edu.cn.

ORCID

Yanfang Meng:0000-0002-4250-650X

Author Contributions

Yanfang Meng was primarily responsible for the experimental design, execution of most experiments, and writing and revision of the manuscript, with other authors providing supplementary experimental support.

Notes

The authors declare no competing financial interest.

Funding Declaration

This work was supported by no Funding

REFERENCES

1 Zhou, J. et al. Fiber-Shaped Photodetectors: Fundamentals, Advances, and Perspectives. Advanced Materials 37, 2504006 (2025).

2 Sun, H. et al. Ultrahigh-Performance Self-Powered Flexible Double-Twisted

Fibrous Broadband Perovskite Photodetector. Advanced Materials 30, 1706986 (2018).

3 Xu, X. et al. A Real-Time Wearable UV-Radiation Monitor Based on a High-Performance p-CuZnS/n-TiO2 Photodetector. Advanced Materials 30, 1803165 (2018).

4 Dong, Y. et al. Self-Powered Fiber-Shaped Wearable Omnidirectional Photodetectors. Nano Energy 30, 173 (2016).

5 Zhang, J. et al. In-Fibre Particle Manipulation and Device Assembly via Laser Induced Thermocapillary Convection. Nature Communications 10, 5206 (2019).

6 Yan, W. et al. Structured Nanoscale Metallic Glass Fibres with Extreme Aspect Ratios. Nature Nanotechnology 15, 875 (2020).

7 Kataria, M. et al. Highly Sensitive, Visible Blind, Wearable, and Omnidirectional Near-Infrared Photodetectors. ACS Nano 12, 9596 (2018).

8 Liu, D. et al. Flexible Omnidirectional Self-Powered Photodetectors Enabled by Solution-Processed Two-Dimensional Layered PbI_2 Nanoplates. ACS Applied Materials & Interfaces 14, 46748 (2022).

9 Fan, H. et al. Continuously Processed, Long Electrochromic Fibers with Multi-Environmental Stability. ACS Applied Materials & Interfaces 12, 28451 (2020).

10 Dang, C. et al. Fibres-Threads of Intelligence-Enable a New Generation of Wearable Systems. Chemical Society Reviews 53, 8790 (2024).

11 Ryu, K.-H. et al. Spacesuit Textiles from Extreme Fabric Materials: Aromatic Amide Polymer and Boron Nitride Nanotube Composite Fiber for Neutron Shielding and Thermal Management. Advanced Fiber Materials 6, 1509 (2024).

12 Peng, H. et al. Ultrahigh Responsivity and Robust Semiconducting Fiber Enabled by Molecular Soldering-Governed Defect Engineering for Smart Textile Optoelectronics. Advanced Materials 36, 2406353 (2024).

13 Fu, Y. et al. Enhanced Property of Flexible UV Photodetectors Based on Electrospinning ZnO-SnO_2 Heterojunction Nanofibers by the Formation of

$Zn2SnO_4$. Ceramics International 49, 11402 (2023).

14 Xue, J. et al. Electrospinning and Electrospun Nanofibers: Methods, Materials, and Applications. Accounts of Chemical Research 50, 1976 (2017).

15 Qian, S. et al. A ‘Moore's law’ for Fibers Enables Intelligent Fabrics. National Science Review 10, nwac023 (2022).

16 Bayindir, M. et al. Metal-Insulator-Semiconductor Optoelectronic Fibres. Nature 431, 826 (2004).

17 Zhu, Z. et al. Improving Wearable Photodetector Textiles via Precise Energy Level Alignment and Plasmonic Effect. Advanced Electronic Materials 3, 1700281 (2017).

18 Li, L. et al. Near-Infrared Light Triggered Self-Powered Mechano-Optical Communication System Using Wearable Photodetector Textile. Advanced Functional Materials 31, 2104782 (2021).

19 Liu, S. et al. A Flexible and Wearable Photodetector Enabling Ultra-Broadband Imaging from Ultraviolet to Millimeter-Wave Regimes. Advanced Science 11, 2401631 (2024).

20 Lu, Z. et al. Integrating High-Sensitivity Photodetector and High-Energy Aqueous Battery in All-in-One Triple-Twisted Fiber. ACS Nano 17, 20087 (2023).

21 Zhu, Z. et al. Fiber-Shaped ZnO/Graphene Schottky Photodetector with Strain Effect. Advanced Materials Interfaces 5, 1800136 (2018).

22 Wan, C. et al. An Artificial Sensory Neuron with Visual-Haptic Fusion. Nature Communications 11, 4602 (2020).

23 Li, C. et al. Polyelectrolyte Elastomer-Based Ionotronic Sensors with Multi-Mode Sensing Capabilities via Multi-Material 3D Printing. Nature Communications 14, 4853 (2023).

24 Mak, K. F. et al. Atomically Thin MoS_2: A New Direct-Gap Semiconductor. Physical Review Letters 105, 136805 (2010).

25 Bernardi, M. et al. Extraordinary Sunlight Absorption and One Nanometer Thick Photovoltaics Using Two-Dimensional Monolayer Materials. Nano Letters 13,

3664 (2013).

26 Radisavljevic, B. et al. Single-Layer MoS_2 Transistors. Nature Nanotechnology 6, 147 (2011).

27 Peng, H. et al. Ultrahigh Responsivity and Robust Semiconducting Fiber Enabled by Molecular Soldering-Governed Defect Engineering for Smart Textile Optoelectronics. Advanced Materials 36, 2406353 (2024).

28 Xiong, Y.-F. et al. A Flexible and Transparent Photodetector Based on Curved Silver Nanowire Network. Advanced Electronic Materials 5, 1800562 (2019).

29 Chen, J.-h. et al. High-sensitivity optical-fiber-compatible photodetector with an integrated $CsPbBr_3$-graphene hybrid structure. Optica 4, 835 (2017).

30 Tang, J. et al. Low Power Flexible Monolayer MoS_2 Integrated Circuits. Nature Communications 14, 3633 (2023).

31 Li, N. et al. Large-Scale Flexible and Transparent Electronics Based on Monolayer Molybdenum Disulfide Field-Effect Transistors. Nature Electronics 3, 711 (2020).

32 Hoang, A. T. et al. Low-Temperature Growth of MoS_2 on Polymer and Thin Glass Substrates for Flexible Electronics. Nature Nanotechnology 18, 1439 (2023).

33 Gant, P. et al. A Strain Tunable Single-Layer MoS_2 Photodetector. Materials Today 27, 8 (2019).

34 Radatović, B. et al. Strain-Enhanced Large-Area Monolayer MoS_2 Photodetectors. ACS Applied Materials & Interfaces 16, 15596 (2024).

35 Lu, D. et al. Strain-Plasmonic Coupled Broadband Photodetector Based on Monolayer MoS_2. Advanced Materials 34, 2107104 (2022).

36 Deng, W. et al. Strain Effect Enhanced Ultrasensitive MoS_2 Nanoscroll Avalanche Photodetector. The Journal of Physical Chemistry Letters 11, 4490 (2020).

37 Arjun, K. et al. Plasmon Induced Ambipolar Photoresponse in Au Decorated MoS_2/PEDOT:PSS Nanocomposite Films. Journal of Applied Physics 135, 214502 (2024).

38 Borgohain, I. P. et al. T Phase Dominant Hybrid 1T/2H@ MoS_2/PEDOT:PSS Nanocomposites for Potential Charge Transport Applications. Journal of Materials

Science 60, 17141 (2025).

39 Vashishtha, P. et al. CVD-Grown Monolayer MoS_2 and GaN Thin Film Heterostructure for a Self-Powered and Bidirectional Photodetector with an Extended Active Spectrum. ACS Applied Materials & Interfaces 16, 31294 (2024).

40 Taffelli, A. et al. MoS_2 Based Photodetectors: A Review. Sensors 21, 2758 (2021).

41 Dodda, A. et al. Stochastic Resonance in MoS_2 Photodetector. Nature Communications 11, 4406 (2020).

42 Kufer, D. et al. Hybrid 2D–0D MoS_2–PbS Quantum Dot Photodetectors. Advanced Materials 27, 176 (2015).

43 An, C. et al. Two-Dimensional Material-Enhanced Flexible and Self-Healable Photodetector for Large-Area Photodetection. Adv. Funct. Mater. 31, 2100136 (2021).

44 Nicolosi, V. et al. Liquid Exfoliation of Layered Materials. Science 340, 1226419 (2013).

45 Aljarb, A. et al. Interfacial Reconstructed Layer Controls the Orientation of Monolayer Transition-Metal Dichalcogenides. ACS Nano 17, 10010 (2023).

46 Fu, D. et al. Molecular Beam Epitaxy of Highly Crystalline Monolayer Molybdenum Disulfide on Hexagonal Boron Nitride. J. Am. Chem. Soc. 139, 9392 (2017).

47 Yang, P. et al. Highly Reproducible Epitaxial Growth of Wafer-Scale Single-Crystal Monolayer MoS_2 on Sapphire. Small Methods 7, 2300165 (2023).

48 Jiang, H. S. et al. Core-Shell Structures for Improved Electrocatalytic Process of Hydrogen Evolution. Journal of Power Sources 472, 228497 (2020).

49 Qin, Q. et al. MoS_2/NiS Yolk-Shell Microsphere-Based Electrodes for Overall Water Splitting and Asymmetric Supercapacitor. Small 15, 1803639 (2018).

50 Jubu, P. R. et al. Tauc-Plot Scale and Extrapolation Effect on Bandgap Estimation from UV–vis–NIR Data – A Case Study of β-Ga2O3. Journal of Solid State Chemistry 290, 121576 (2020).

51 Wei, Q. et al. Morphological Change and Mobility Enhancement in PEDOT:PSS

by Adding Co-Solvents. Advanced Materials 25, 2831 (2013).

52 Kind, H. et al. Nanowire Ultraviolet Photodetectors and Optical Switches. Advanced Materials 14, 158 (2002).

53 Wang, H. et al. Low-Dimensional Metal Halide Perovskite Photodetectors. Advanced Materials 33, 2003309 (2021).

54 Wang, Z. X. et al. High-quality semiconductor fibres via mechanical design. Nature 626, 72 (2024).

55 Tang, X. et al. PEDOT:PSS for Piezophototronic Effect-Enhanced Self-Powered Flexible Photodetectors. Nano-Micro Letters 17, 56 (2025).

56 Li, H. et al. Promising Hybrid Graphene-Silver Nanowire Composite Electrode for Flexible Organic Light-Emitting Diodes. Scientific Reports 5, 17998 (2015).

57 Wang, P. et al. Highly Stable Graphene-Based Flexible Hybrid Transparent Conductive Electrodes for Organic Solar Cells. Advanced Materials Interfaces 9, 2101442 (2022).

58 Hao, T. et al. Capillary Force-Induced Graphene Spontaneous Transfer and Encapsulation of Silver Nanowires for Highly-Stable Transparent Electrodes. ACS Applied Materials & Interfaces 16, 40199 (2024).

59 Harm, O. et al. Title of the Article. Nano Letters 25, 17556 (2025).

60 Zhu, H. et al. Observation of piezoelectricity in free-standing monolayer MoS_2. Nature Nanotechnology 10, 151 (2015).

61 Tan, D. et al. Prediction of strong piezoelectricity in 3R- MoS_2 multilayer structures. Nano Energy 56, 512 (2019).

62 Hallil, H. et al. Strong Piezoelectricity in 3R- MoS_2 Flakes. Advanced Electronic Materials 8, 2101147 (2022).

63 Zheng, S. et al. Anomalous Reconfigurable-Transport in MoS_2 Transistors by Electrically-Switchable van der Waals Interfacial Dipole. Advanced Materials 37, e02784 (2025).

64 Robertson, J. et al. Extending the metal-induced gap state model of Schottky barriers. Journal of Vacuum Science & Technology B 38, 042208 (2020).

65 Chen, X. et al. Probing the electron states and metal-insulator transition mechanisms in molybdenum disulphide vertical heterostructures. Nature Communications 6, 6088 (2015).

66 Wang, X. et al. Simple Layer-by-Layer Assembly Method for Simultaneously Enhanced Electrical Conductivity and Thermopower of PEDOT:PSS/ce- MoS_2 Heterostructure Films. ACS Applied Energy Materials 1, 3123 (2018).

67 Yuan, S. et al. A High Environmentally Stable Ionic Hydrogel for Pressure-Temperature Bimodal Passive Flexible Tactile Sensor. Advanced Functional Materials 36, e15806 (2026).

68 Bai, C. et al. A self-powered hydrogel electronic skin with decoupled multimodal sensing for closed-loop human-machine interactions. Nature Communications 17, 2675 (2026).

69 Yang, Q. et al. Machine Learning-Enhanced Modular Ionic Skin for Broad-Spectrum Multimodal Discriminability in Bidirectional Human–Robot Interaction. Advanced Materials 37, e08795 (2025).

70 Zhou, X. et al. Coaxial Hydrogel Optical Fibre Skin for Interference-Free Multimodal Tactile Perception. Advanced Materials 38, e72869 (2026).

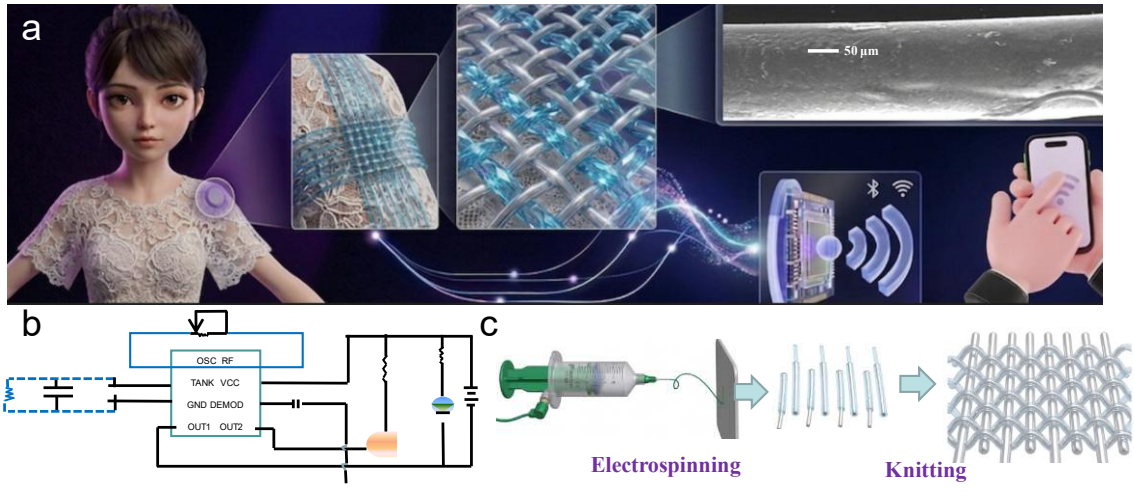


Figure 1 (a) The schematically diagram of the schematically diagram of the operational concept of the proposed textile-integrated heterojunction photodetector array with the enlarged scheme of photodetector array and the magnified Scanning electron

microscopy (SEM). **(b)** Circuit diagram of fiber-shaped photodetector array **(c)** Schematic diagram of the fabrication process of MoS_2/PEDOT:PSS heterojunction fiber-shaped photodetector array

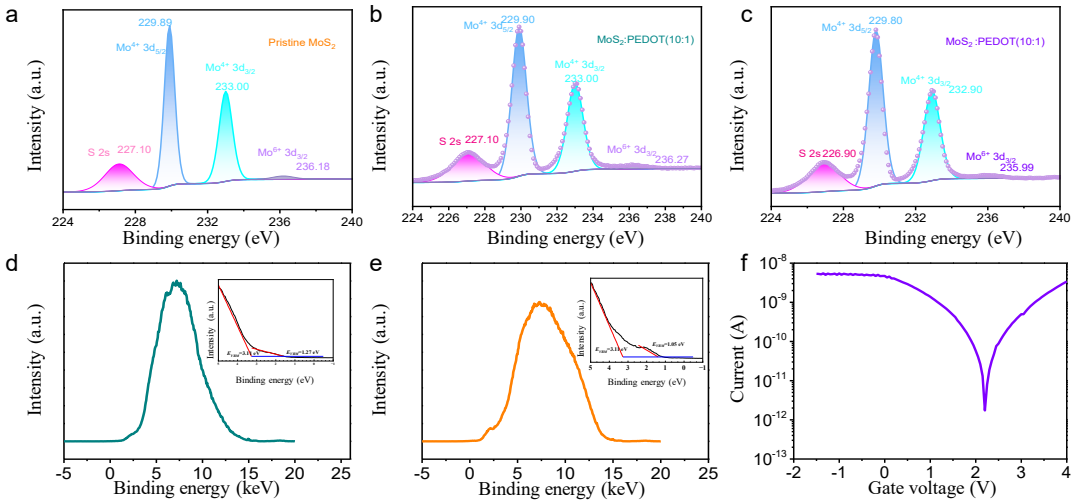


Figure 2 (a)-(c) Mo^{4+} $3d_{5/2}$, Mo^{4+} $3d_{5/2}$ and Mo^{4+} $3d_{5/2}$ XPS spectra of pristine MoS_2 film, MoS_2/PEDOT(20:1) film, and MoS_2/PEDOT(10:1) film. **(d)** UPS of pristine MoS_2 crystalline (e) UPS of MoS_2/PEDOT(20:1) composite. **(f)** the transfer curve of MoS2/PEDOT:PSS heterojunction

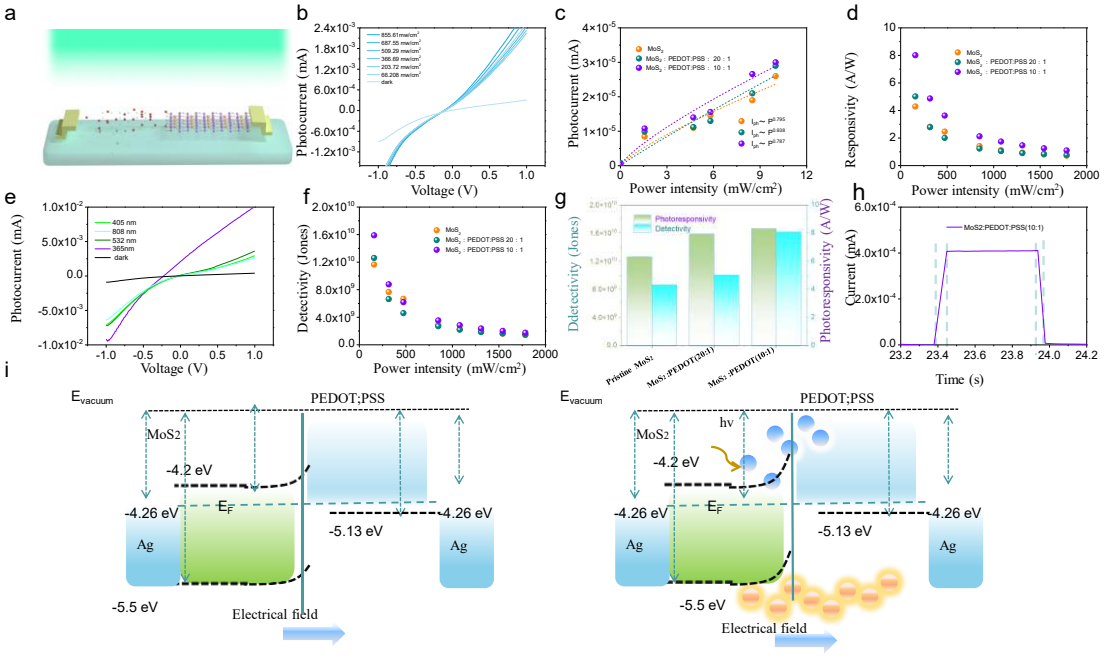


Figure 3 (a) the scheme of planar configuration of MoS_2/PEDOT:PSS heterojunction measured at a source-drain voltage of 2 V (b) The voltage-dependent photocurrent of the MoS_2/PEDOT(20:1) device under 365 nm at varying power 66.3 mW/cm^2 **(c)** The power-dependent photoresponsivity (R) of the pristine MoS_2 film, MoS_2/PEDOT (20:1) film, and MoS_2/PEDOT(10:1) film under 365 nm at 66.3 mW/cm^2 (bias voltage 0.01 V) **(d)** The power-dependent photocurrent of the pristine MoS_2 film, MoS_2/PEDOT(20:1) film, and MoS_2/PEDOT(10:1) film under 365 nm at 66.3 mW/cm^2 (bias voltage 0.01 V) **(e)** The measured response of three samples under similar incident power levels (at the given wavelength of 365 nm at 157 mW/cm^2, the 405 nm at 66.3 mW/cm^2 the 365 nm at 66.3 mW/cm^2). **(f)** The relationship of detectivity and illumination intensity 365 nm at 66.3 mW/cm^2, 315.35 mW/cm^2, 473.19 mW/cm^2, 847.53 mW/cm^2, and 1078.86 mW/cm^2 (bias voltage 0.01 V) **(g)** The relationship of detectivity and illumination intensity 405 nm at 66.2 μW/cm², 203.72 μW/cm², 366.69 μW/cm², 509.29 μW/cm², and 687.55 μW/cm² (bias voltage 0.01 V) **(h)** Comparison of photoresponsivity (*R*) and detectivity (*D*) as a function of illumination intensity for pristine MoS_2 and MoS_2/PEDOT:PSS heterojunction devices at the given wavelength of 365 nm at 157 mW/cm^2 of the device at a rise time and a fall behavior (bias voltage 0.01 V). **(i)** Schematic illustration of the mechanism of photocurrent generation begins with photoexcitation, where absorbed photons create electron-hole pairs. These charge carriers are then separated and driven to drift by an applied bias, thereby generating a measurable photocurrent.

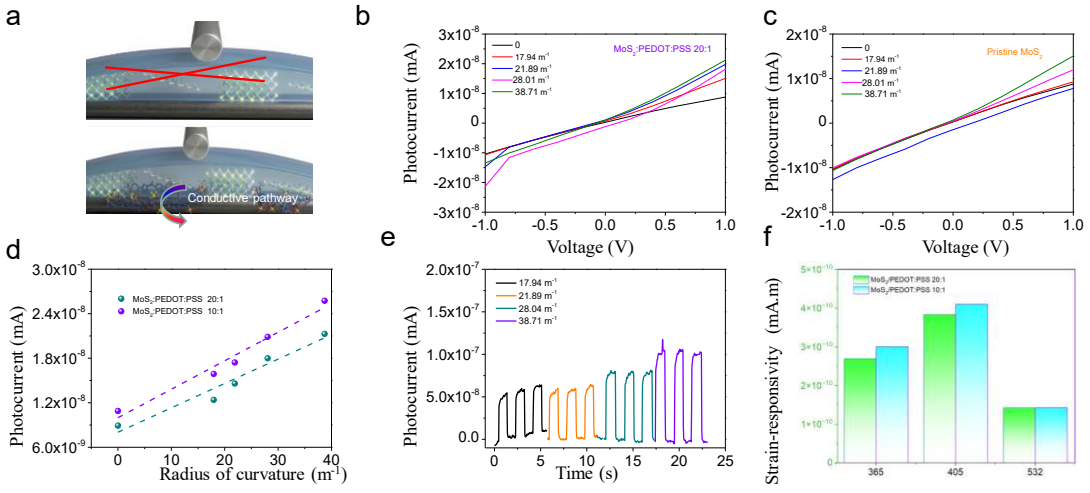


Figure 4 (a) Upper panel: schematic illustration of the MoS_2 heterojunction device under bending, where conductive channels is unavailable, Bottom panel: schematic illustration of the MoS_2/PEDOT:PSS heterojunction device under bending, where, PEDOT:PSS serves as a conductive bridge to establish a continuous pathway. **(b)** The strain-dependent photocurrent of the pristine MoS_2 devices under 405 nm 66.3 mW/cm^2 **(c)** The strain-dependent photocurrent of the pristine MoS_2/PEDOT:PSS heterojunction device under 405 nm 66.3 mW/cm^2 the linear relationships between photocurrent and curvature radius inserted **(d)** The comparison of the linear relationships between photocurrent and curvature radius of pristine MoS_2 and MoS_2/PEDOT:PSS(10:1) heterojunction devices. **(e)** The real-time strain-dependent photocurrent of the devices under 405 nm 66.3 mW/cm^2 **(f)** The comparison of the linear relationships between photocurrent and curvature radius of pristine MoS_2 and MoS_2/PEDOT:PSS(10:1) heterojunction devices.

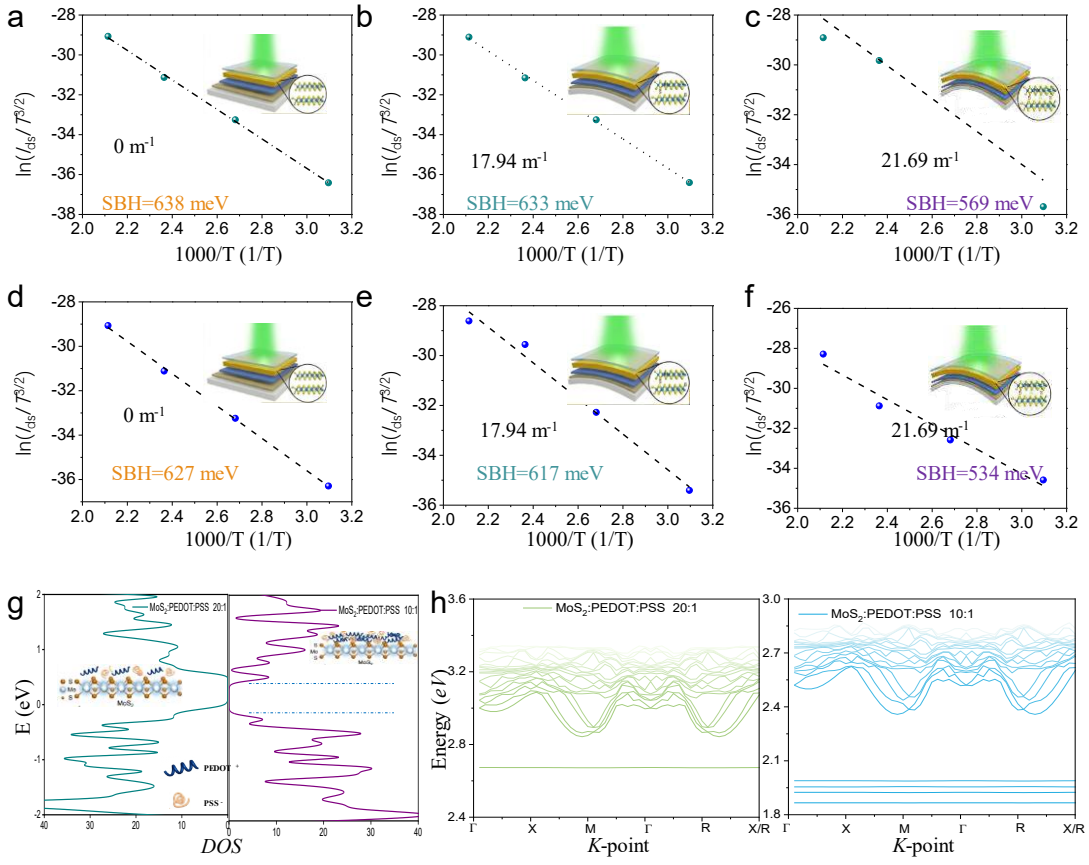


Figure 5 (a), (b), (c) Arrhenius plots for MoS_2/PEDOT:PSS(20:1) heterojunctions

under planar configuration, bending curvatures radii 17.94 m^{-1}, and 38.71 m^{-1}, respectively. **(d)**, **(e)**, **(f)** Arrhenius plots for MoS_2/PEDOT:PSS(10:1) heterojunctions under planar configuration, bending curvatures radii 17.94 m^{-1}, and 38.71 m^{-1}, respectively. **(g)** First-principles calculation on PEDOT:PSS effect on the modulation for the electronic environment of MoS_2/PEDOT:PSS(20:1)(left panel) and MoS_2/PEDOT:PSS(10:1)(right panel). **(h)** First-principles calculation on projected band structure of MoS_2/PEDOT:PSS(20:1)(left panel) and MoS_2/PEDOT:PSS(10:1)(right panel).

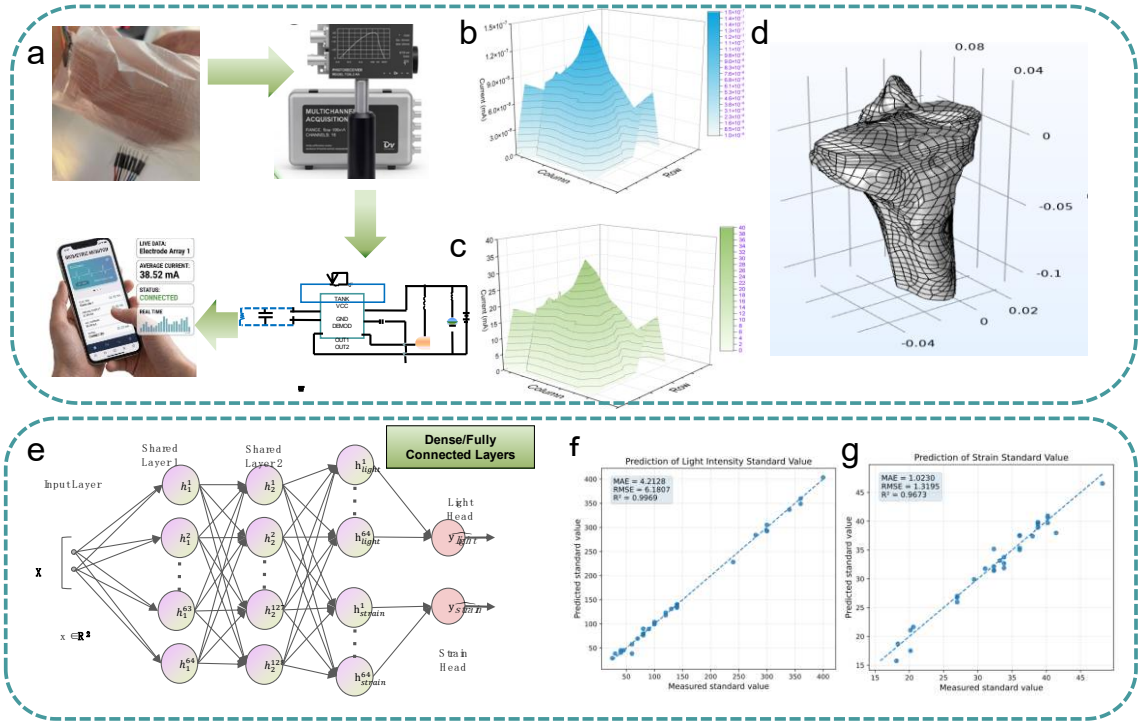


Figure 6 MoS_2/PEDOT:PSS heterojunction fiber-shaped photodetector array **(a)** Upper left panel: the photograph of the device attached to the elbow joint. When the array was closely attached to the elbow joint, the sensing signals collected by (upper right panel) were determined by the equivalent terminal voltage applied to the ends of the crisscrossing fibers. The collected signals were amplified by a signal converter circuit (bottom left panel) and transmitted via Bluetooth to a mobile receiver (bottom right panel). **(b)** The output photocurrents were measured and visualized in a 3D colour coordinate map. **(c)** The extracted strain distribution of elbow joint from Figure 6b in a 3D colour coordinate map **(d)** COMSOL simulation

of strain distribution of elbow joint. **(e)** Illustration of the principle of the framework architecture for decoupling in deep learning **(f)-(g)** FPD signals decoupling under large bending strain: prediction of light density standard values **(f)**; prediction of strain standard values **(g)**.

Supplementary Files

This is a list of supplementary files associated with this preprint. Click to download.

- supportinginformation.docx